Global thrust faulting on the Moon and the influence of tidal stresses

Thomas R. Watters[1]*, Mark S. Robinson[2], Geoffrey C. Collins[3], Maria E. Banks[1], Katie Daud[1], Nathan R. Williams[2], and Michelle M. Selvans[1]

[1]Center for Earth and Planetary Studies, Smithsonian Institution, Washington, D.C. 20560, USA
[2]School of Earth and Space Exploration, Arizona State University, Tempe, Arizona 85251, USA
[3]Physics and Astronomy Department, Wheaton College, Norton, Massachusetts 02766, USA

ABSTRACT

Lunar Reconnaissance Orbiter Camera images reveal a vast, globally distributed network of over 3200 lobate thrust fault scarps, making them the most common tectonic landform on the Moon. Based on their small scale and crisp appearance, crosscutting relations with small-diameter impact craters, and rates of infilling of associated small, shallow graben, these fault scarps are estimated to be younger than 50 Ma and may be actively forming today. The non-random distribution of the scarp orientations is inconsistent with isotropic stresses from late-stage global contraction as the sole source of stress. We propose that tidal stresses contribute significantly to the current stress state of the lunar crust. Orbital recession stresses superimposed on stresses from global contraction with the addition of diurnal tidal stresses result in non-isotropic compressional stress and thrust faults consistent with lobate scarp orientations. The addition of diurnal tidal stresses at apogee result in peak stresses that may help trigger coseismic slip events on currently active thrust faults on the Moon.

INTRODUCTION

Tectonic landforms described as lobate scarps are common on the terrestrial planets (Watters, 2003; Watters et al., 2009; Watters and Schultz, 2010). The morphology, crosscutting relations, reversals in vergence, segment linkage, and modeling all suggest that lobate scarps express contraction of crustal materials and are formed by thrust faults (Schultz, 1976; Binder, 1982; Watters and Johnson, 2010; Watters et al., 2010). Some lobate scarp thrust faults on Mercury and Mars are on a scale with the largest thrust fault structures on Earth (e.g., the Wind River Mountains, Wyoming, USA), with over a kilometer of relief and hundreds of kilometers in length (Watters, 2003; Watters et al., 2009). Lunar lobate scarps, in contrast, are relatively small-scale landforms, typically <10 km in length with only tens of meters of relief (Fig. 1A) (Watters and Johnson, 2010; Watters et al., 2010; Banks et al., 2012). Fault dislocation modeling constrains the maximum depth of the associated thrust faults to be within the upper kilometer of the lunar megaregolith (Williams et al., 2013).

In Apollo mission–era studies, the number and global distribution of lunar scarps were unknown (Watters et al., 2010) because the high-resolution Lunar Orbiter and Apollo Panoramic Camera photographs were limited in coverage to only a portion of the lunar equatorial zone (Schultz, 1976; Binder, 1982). Currently, over one million images of the lunar surface have been acquired by the Lunar Reconnaissance Orbiter Camera (LROC) Wide Angle Camera (WAC) and Narrow Angle Cameras (NACs) (Robinson et al., 2010). The pixel scale of NAC images (0.5–2.0 m/pixel) is ideal for the detection of the small-scale landforms (Watters et al., 2010; Banks et al., 2012). We show the global distribution and orientations of the emerging population of lunar thrust fault scarps and investigate causal stresses by comparing predicted tidal
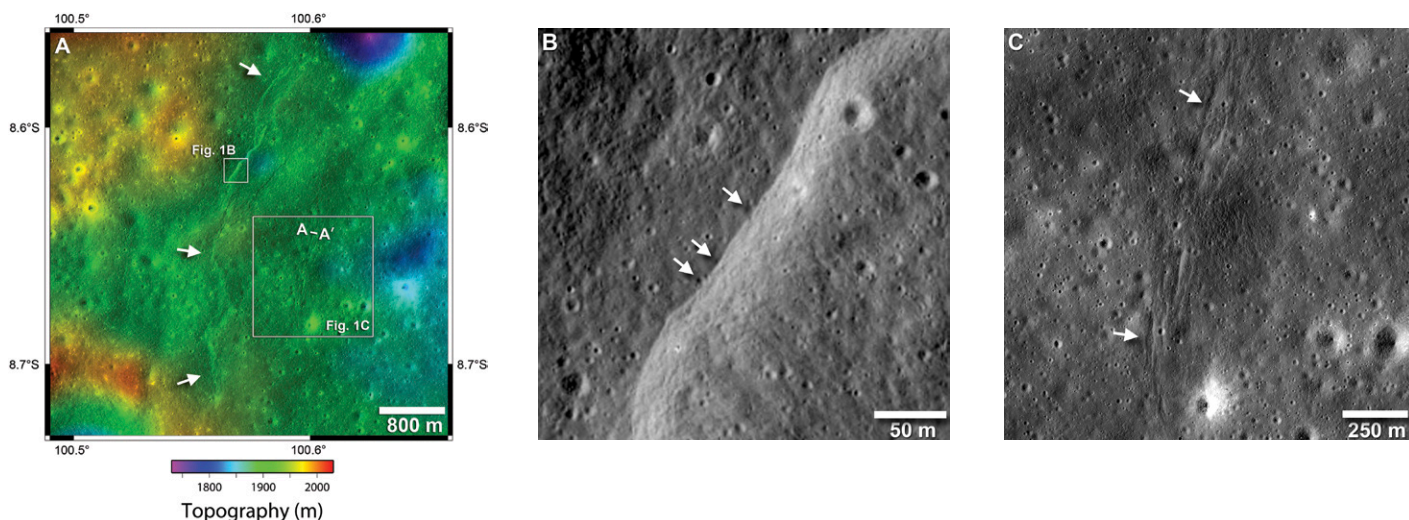
Figure 1. A: Digital elevation model of Pasteur scarp generated using Lunar Reconnaissance Orbiter Camera (LROC) Narrow Angle Camera (NAC) stereo images (frames M1113517026 and M1113502820). Pasteur scarp (white arrows) is located in nearside highlands (~8.6°S, 100.6°E), and has maximum relief of ~20 m. Located ~1.2 km from the scarp face are small-scale graben (see C). Digital elevation model has a horizontal spatial scale of 4 m/pixel (NAC stereo images have resolution of ~1 m/pixel) and vertical precision of ~0.5 m (see the Data Repository [see footnote 1]). Topographic profile across a graben (A–A′) is shown in Figure DR1 (see footnote 1). Elevations are referenced to sphere of 1,737,400 m radius. B: Segment of Pasteur scarp crosscutting small-diameter impact craters. Craters ~4–7 m in diameter (white arrows) are crosscut or disturbed by the lobate scarp. Craters this small are estimated to be no older than 800 Ma. Figure location is shown in A. LROC NAC frame M1113517026. C: Graben (white arrows) associated with highland Pasteur scarp. Pasteur graben are oriented sub-parallel to scarp face and extend for ~1.5 km with the largest ~300 m in length and ~20–30 m wide, while some graben have widths of <10 m. Shallow graben formed in regolith would be expected to disappear in <50 m.y. Figure location is shown in A. LROC NAC frame M1113517026.

*E-mail: watterst@si.edu

stresses in combination with global contraction due to interior cooling. (Further information is available in the GSA Data Repository[1].)

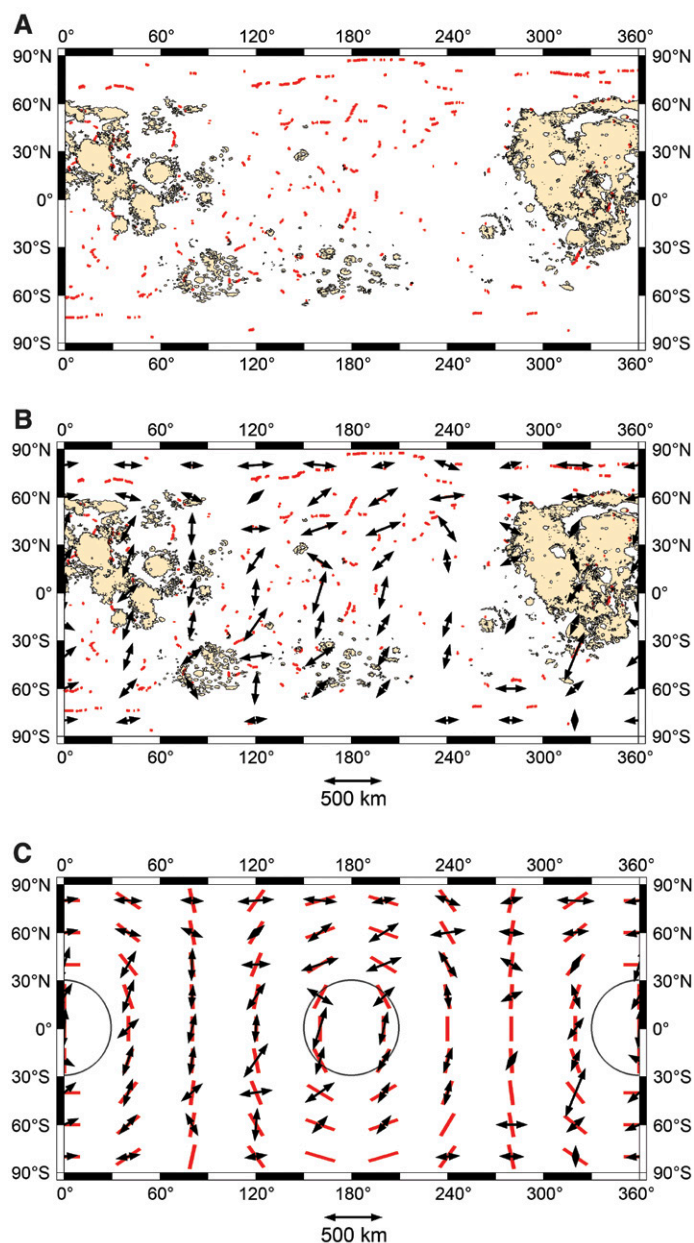## AGE AND SPATIAL DISTRIBUTION OF LUNAR LOBATE SCARPS

Lobate scarps are thought to be relatively young landforms due to the lack of superposed relatively large-diameter (>400 m) impact craters, their generally crisp morphology, and crosscutting relations with small-diameter impact craters (<50 m in diameter) (Fig. 1B) (Binder, 1982; Watters et al., 2010). Impact craters with diameters of <50 m are estimated to be no older than 800 ± 15 Ma (Copernican age) (Trask, 1971; Stöffler and Ryder, 2001). Small-scale extensional troughs or graben with depths as shallow as 1–2 m are locally found in back-limb areas of the scarps and are likely a consequence of flexural bending (Fig. 1C; Fig. DR1 in the Data Repository) (Watters et al., 2012). Shallow troughs in the lunar regolith are estimated to fill in at a rate of 5 ± 3 cm/m.y., based on analysis of boulder tracks (Arvidson et al., 1975). Thus, shallow graben formed in regolith are expected to disappear in <50 m.y., consistent with the interpretation that lobate scarps are young tectonic landforms (Watters et al., 2012). Young faults may also be consistent with recorded lunar seismic activity. Although the majority of the recorded moonquakes were deep within the interior, triggered in part by tidal stresses (Weber et al., 2009), 28 were shallow (<100 km depth; see Nakamura et al., 1979; Watters and Johnson, 2010).

LROC NAC images obtained to date cover >70% of the lunar surface with complete coverage of the polar regions (within 20° latitude of the poles) except in permanently shadowed regions. The locations of lobate scarps identified in an ongoing survey of these images were digitized directly from map-projected, 2 m pixel–scale NAC mosaics and 100 m pixel–scale WAC monochrome mosaics. NAC images with large incidence angles (>50°; see the Data Repository) are optimum for identifying and digitizing the lobate scarps. Over 3200 scarps were digitized, with each scarp divided into segments with uniform orientations and minimum segment lengths of ~200 m (Fig. 2) (see the Data Repository). Lobate scarps are globally distributed, confirming predictions based on earlier, sparse surveys (Watters et al., 2010; Banks et al., 2012). Their occurrence at all latitudes on both the nearside and farside makes them the most common and broadly distributed tectonic landform on the Moon. A small fraction of lobate scarps are found in mare basalts (~3% of mapped scarps), but they occur primarily in the lunar highlands where they are the dominant tectonic landform (Fig. 2A). Some lobate scarps (~4% of those mapped) occur in highlands at the margins of the mare units. One explanation for the disproportionately small number of lobate scarps in maria may be the preference for wrinkle ridges, more complex contractional features, to form in the multilayered mare basalts (see Watters and Johnson, 2010). Although the longest individual scarps typically reach maximum lengths up to only a few tens of kilometers, clusters of scarps in linear and curvilinear patterns may extend for several hundred kilometers (Fig. 2A).

DISTRIBUTION OF SCARP ORIENTATIONS

The orientations of the fault scarps were evaluated by sampling the digitized segments in areas with dimensions of 40° longitude × 20° latitude. The median orientations were plotted and scaled by the total length of the structures within the sampled areas (Fig. 2B). The overall pattern reveals that the orientations of many scarps are broadly north-south at low to mid-latitudes and east-west at high latitudes. This could be due to observational bias where features oriented perpendicular to the local illumination direction are expected to be preferentially enhanced, because at the equator the illumination direction is east or west and at the poles the illu-

Figure 2. A: Map of digitized locations of lobate scarps on the Moon. Over 3200 lunar scarps (red) have been mapped. Mare basalt units are shown in tan. B: Plot of median orientations of lobate scarps (black double arrows) sampled in areas with dimensions of 40° longitude × 20° latitude and scaled by total length of structures in sampled areas. Each digitized scarp consists of a polyline, a connected series of linear segments. Orientation of each segment is used to determine median orientation of scarps in sampled area (see Table DR1 [see footnote 1]). Mare basalt units are shown in tan. C: Orientations of predicted faults (red lines) due to combination of recession stresses, diurnal tidal stresses at apogee, and global contraction plotted with median orientations of lobate scarps (black double arrows). Predicted fault trajectories correspond to the orthogonal to the most compressive stress directions. Sub-Earth and anti-Earth regions are shown by black circles.

mination direction is north or south. However, significant deviations from north-south orientations are common at the low to mid-latitudes (Fig. 2B). Even at high latitudes (±60° and poleward) where the dominant orientations are more east-west, north-south–oriented scarps are found (see the Data Repository; Fig. DR2). Thus, while the influence of illumination bias cannot be disregarded, the pattern of orientations of the lobate scarps is not

dominated by this effect. Other influences, however, may locally affect the orientation of the scarps, most notably the nearside mare basins. Lobate scarps associated with mare commonly occur near the contact between the mare basalts and highland material with orientations that parallel the basin margins (Watters and Johnson, 2010). This proximity suggests that mechanical heterogeneities and boundary effects introduced by the mare basins influenced the orientations of the lobate scarps at basin margins on the nearside.

ORIGIN OF STRESSES

Thermal history models for an initially totally molten Moon (Binder and Gunga, 1985; Binder, 1986; Pritchard and Stevenson, 2000) or an early Moon with a near-surface magma ocean (Solomon and Head, 1979, 1980; Solomon, 1986) both predict late-stage global contraction. The early cessation of basin-related flexural extension from loading by mare basalts, not long after the end of the period of late heavy bombardment (ca. 3.8 Ga) (Lucchitta and Watkins, 1978; Boyce, 1976; Hiesinger et al., 2000, 2003), may be due to the superposition of compressional stresses from global contraction, marking a transition in the Moon's thermal history where interior cooling resulted in a shift from net expansion to net contraction (Solomon and Head, 1979, 1980; Solomon, 1986). The magnitude of compressional stress from a small sample of the young thrust faults was previously estimated to be <10 MPa (Watters et al., 2010; Watters and Johnson, 2010), consistent with low levels of post–late heavy bombardment compressional stress predicted by magma ocean thermal models (Solomon and Head, 1979, 1980; Solomon, 1986). Using the population of fault scarps described in this global study, the contractional strain is estimated to be equivalent to a radius change of ~25 m corresponding to isotropic stresses of ~2 MPa (see Watters and Johnson, 2010). This is a minimum stress because the entire population of fault scarps has yet to be mapped. Based on strength envelopes for near-surface lunar regolith, stresses of ~2–7 MPa are sufficient for shallow thrust faults (upper few hundred meters depth) to develop (see Williams et al., 2013).

In the absence of other influences, global contraction will result in horizontally isotropic compressional stresses. Such a stress field is expected to form a population of thrust faults that are more or less uniformly distributed but with random orientations. However, the distribution of orientations of mapped lobate scarps is non-random (Fig. 2) (weighted vector mean ~9.0°, circular standard deviation 54.3°, n = 51,614 digitized segments), and thus their orientations are not consistent with global contraction as the sole source of compressional stress. Mechanical inhomogeneities introduced by the nearside mare basins and perhaps by heavily degraded rims of ancient farside basins (Frey, 2011) may play a role in locally orienting the stresses, but the distribution of orientations suggests that other global-scale stresses have influenced the formation of the thrust faults.

TIDAL STRESSES

Relaxation of early lunar tidal and rotational bulges from despinning and orbital recession may have been a source of global stress. Melosh (1980) examined these effects, and the predicted stresses are expected to result in contraction and north-south–oriented thrust faults in the region in and around the sub-Earth and anti-Earth points, a system of strike-slip faults at low to mid-latitudes outside sub- and anti-Earth areas, and extension and east-west–oriented normal faulting in the polar regions (Melosh, 1980; Collins et al., 2010). In addition to the absence of evidence for strike-slip and poleward normal faults, tidal despinning likely peaked early in the Moon's evolution. Continued, slow orbital recession, however, contributes significantly to the current stress state of the Moon, and the magnitude of this stress is a function of h_2, the Love number defining the vertical displacement in response to a gravitational potential, and the distance the satellite has receded over a period of time (Melosh, 1980; Collins et al., 2010) (see the Data Repository). On short time scales, recession

stresses are small. However, if recession stresses have accumulated over a long period, much greater than the age of the thrust faults, they may be considerably larger. Also, h_2 has likely significantly decreased with time to its present value (~0.04; Mazarico et al., 2014; Williams and Boggs, 2015) as the lunar interior has cooled and increased in rigidity. Thus, the maximum recession stresses at the sub- and anti-Earth points could be ~20–40 kPa for an h_2 of 0.04–0.08 (as much as twice the present value) for a period of recession of 1.2 b.y. (see Fig. DR3).

Another component of the current state of stress of the Moon is Earth-raised solid body tides (Watters et al., 2010). The Moon is a tidally locked (synchronous orbit) satellite with nonzero orbital eccentricity. Thus, as the Moon moves from perigee (closest distance) to apogee (farthest distance), diurnal tidal stresses are induced by the Earth. The amplitude of the diurnal tidal budge is small, on the order of only ~10–20 cm as determined using Lunar Orbiter Laser Altimeter (LOLA) ranging (Mazarico et al., 2014). The maximum diurnal stress is proportional to $3EeH/R_m$ where e is the orbital eccentricity, R_m is the radius of the Moon, E is Young's modulus, and H is the static tidal bulge amplitude, which is related to h_2 (Collins et al., 2010; Murray and Dermott, 1999). The magnitude of the diurnal stress is low (maximum of ≤5 kPa) compared to those from orbital recession and global contraction. While diurnal stresses are compressional in the region around the sub-Earth and anti-Earth points at apogee, the stresses oscillate with the Moon's orbital position, becoming extensional at the same locations at perigee.

The current stress state of the lunar crust thus consists of at least three global components: diurnal tidal stress σ_t, orbital recession stress σ_r, and global contraction σ_c. Orbital recession and diurnal tidal stresses, although relatively small, superimposed on stresses from global contraction will result in a net non-isotropic compressional stress field σ_n where $\sigma_c \gg \sigma_r > \sigma_t$. The non-isotropic compressional stress σ_n is expected to result in thrust faulting with preferred orientations (Fig. 2C; Fig. DR5). Although the ratio of the maximum stress from global contraction to the stress from orbital recession is large (up to ~100 depending on the assumed time scale and h_2 value; see Fig. DR3), the small non-isotropic stresses may control thrust fault orientations in regions that are otherwise mechanically homogeneous. As a test of this hypothesis, the orientation of each mapped fault segment was compared to the local orientation of the principal axis of most compressive stress calculated from three general models: orbital recession, despinning, and orbital recession with added diurnal tides. If the tidal stresses are influencing the fault population, the expected faults would be close to perpendicular to the local axis of most compressive stress. The predicted fault orientations from all three models are generally in good agreement with the observed orientations of the lobate scarps and are markedly different from a simulated population of faults with random orientations from isotropic contraction (Fig. 3). None of the models is a perfect fit, with a significant fraction (36%–40%) of the faults more than 45° from the expected local orientation. With such a small organizing stress superimposed on isotropic contraction, such deviations should be expected due to a variety of influences (see the Data Repository). Overall, the pattern of preferred orientations of the population of young thrust fault scarps is best accounted for by recession stresses added to the stress due to global contraction (Fig. 3). Recession stresses combined with the diurnal stress at apogee result in an almost equally good fit (Fig. 3). Stresses due to recession do not change with orbital position, thus it is the combination of recession and contraction stresses that dominate throughout the Moon's orbit, with peak compressional stresses reached by the addition of diurnal stresses at apogee.

Because the magnitude of σ_n is the greatest at apogee when diurnal and recession stresses are most compressive, coseismic slip on the thrust faults may preferentially occur during this time. If the population of thrust faults is still active, the occurrence of shallow seismic events may be greater when the Moon is at apogee. This hypothesis can be tested when the International Lunar Network is deployed.
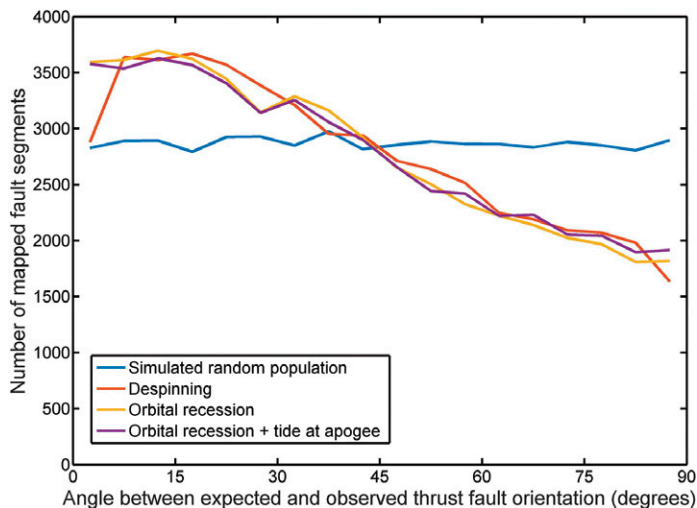
Figure 3. Agreement between observed faults and expected local thrust fault orientations due to different stress models. Fault segments at 0° on plot are orthogonal to local direction of most compressive stress, and at 90° they are parallel to most compressive stress. Red line shows expected orientations for decrease in spin rate; yellow line shows expected orientations for lowering of tidal and rotational distortions as the Moon recedes from Earth; purple line shows stresses from recession added to diurnal tidal stress at apogee (see the Data Repository [see footnote 1]). For reference, blue line shows simulated fault population with same total number of fault segments but with random orientations, as may be expected under an isotropic stress field. Angular differences are sampled in 5° bins.

REFERENCES CITED
Arvidson, R., Drozd, R.J., Hohenberg, C.M., Morgan, C.J., and Poupeau, G., 1975, Horizontal transport of the regolith, modification of features, and erosion rates on the lunar surface: The Moon, v. 13, p. 67–79, doi:10.1007/BF00567508.

Banks, M.E., Watters, T.R., Robinson, M.S., Tornabene, L.L., Tran, T., Ojha, L., and Williams, N.R., 2012, Morphological analysis of lobate scarps on the Moon using data from the Lunar Reconnaissance Orbiter: Journal of Geophysical Research, v. 117, E00H11, doi:10.1029/2011JE003907.

Binder, A.B., 1982, Post-Imbrian global lunar tectonism: Evidence for an initially totally molten moon: Earth, Moon, and Planets, v. 26, p. 117–133, doi:10.1007/BF00929277.

Binder, A.B., 1986, The initial thermal state of the Moon, in Hartmann, W.K., et al., eds., Origin of the Moon: Houston, Texas, Lunar and Planetary Institute, p. 425–433.

Binder, A.B., and Gunga, H.-C., 1985, Young thrust-fault scarps in the highlands: Evidence for an initially totally molten Moon: Icarus, v. 63, p. 421–441, doi:10.1016/0019-1035(85)90055-7.

Boyce, J.M., 1976, Ages of flow units in the lunar nearside maria based on Lunar Orbiter IV photographs, in Proceedings, Seventh Lunar Science Conference, Houston, Texas, 15–19 March: Oxford, UK, Pergamon Press, p. 2717–2728.

Collins, G.C., McKinnon, W.B., Moore, J.M., Nimmo, F., Pappalardo, R.T., Prockter, L.M., and Schenk, P.M., 2010, Tectonics of the outer planet satellites, in Watters, T.R., and Schultz, R.A., eds., Planetary Tectonics: New York, Cambridge University Press, p. 264–350.

Frey, H., 2011, Previously unknown large impact basins on the Moon: Implications for lunar stratigraphy, in Ambrose, W.A., and Williams, D.A., eds., Recent Advances and Current Research Issues in Lunar Stratigraphy: Geological Society of America Special Paper 477, p. 53–75, doi:10.1130/2011 .2477(02).

Hiesinger, H., Jaumann, R., Neukam, G., and Head, J.W., 2000, Ages of mare basalts on the lunar nearside: Journal of Geophysical Research, v. 105, p. 29,239–29,276, doi:10.1029/2000JE001244.

Hiesinger, H., Head, J.W., Wolf, U., Jaumann, R., and Neukam, G., 2003, Ages and stratigraphy of mare basalts in Oceanus Procellarum, Mare Nubium, Mare Cognitum, and Mare Insularum: Journal of Geophysical Research, v. 108, 5065, doi:10.1029/2002JE001985.

Lucchitta, B.K., and Watkins, J.A., 1978, Age of graben systems on the Moon, in Proceedings, Ninth Lunar and Planetary Science Conference, Houston, Texas, 3–17 March: Oxford, UK, Pergamon Press, p. 3459–3472.

Mazarico, E.M., Barker, K., Neumann, G.A., Zuber, M.T., and Smith, D.E., 2014, Detection of the lunar body tide by the Lunar Orbiter Laser Altimeter: Geophysical Research Letters, v. 41, p. 2282–2288, doi:10.1002/2013GL059085.

Melosh, H.J., 1980, Tectonic patterns on a tidally distorted planet: Icarus, v. 43, p. 334–337, doi:10.1016/0019-1035(80)90178-5.

Murray, C.D., and Dermott, S.F., 1999, Solar System Dynamics: New York, Cambridge University Press, 592 p.

Nakamura, Y., Latham, G.V., Dorman, H.J., Ibrahim, A.-B.K., Koyama, J., and Horvath, P., 1979, Shallow moonquakes–Depth, distribution and implications as to the present state of the lunar interior, in Proceedings, 10th Lunar and Planetary Science Conference, Houston, Texas, 19–23 March: Oxford, UK, Pergamon Press, p. 2299–2309.

Pritchard, M.E., and Stevenson, D.J., 2000, Thermal aspects of a Lunar origin by giant impact, in Canup, R., and Righter K., eds., Origin of the Earth and Moon: Tucson, University of Arizona Press, p. 179–196.

Robinson, M.S., et al., 2010, Lunar Reconnaissance Orbiter Camera instrument overview: Space Science Reviews, v. 150, p. 81–124, doi:10.1007/s11214-010-9634-2.

Schultz, P.H., 1976, Moon Morphology: Interpretations Based on Lunar Orbiter Photography: Austin, University of Texas Press, 626 p.

Solomon, S.C., 1986, On the early thermal state of the Moon, in Hartmann, W.K., et al., eds., Origin of the Moon: Houston, Texas, Lunar and Planetary Institute, p. 435–452.

Solomon, S.C., and Head, J.W., 1979, Vertical movement in mare basins: Relation to mare emplacement, basin tectonics, and lunar thermal history: Journal of Geophysical Research, v. 84, p. 1667–1682, doi:10.1029/JB084iB04p01667.

Solomon, S.C., and Head, J.W., 1980, Lunar mascon basins: Lava filling, tectonics, and evolution of the lithosphere: Reviews of Geophysics and Space Physics, v. 18, p. 107–141, doi:10.1029/RG018i001p00107.

Stöffler, D., and Ryder, G., 2001, Stratigraphy and isotope ages of lunar geologic units: Chronological standard for the inner solar system: Space Science Reviews, v. 96, p. 9–54, doi:10.1023/A:1011937020193.

Trask, N.J., 1971, Geologic comparison of mare materials in the lunar equatorial belt, including Apollo 11 and Apollo 12 landing sites, in Geological Survey Research 1971, Chapter D: U.S. Geological Survey Professional Paper 750-D, p. D138–D144.

Watters, T.R., 2003, Thrust faulting along the dichotomy boundary in the eastern hemisphere of Mars: Journal of Geophysical Research, v. 108, 5054, doi:10.1029/2002JE001934.

Watters, T.R., and Johnson, C.L., 2010, Lunar Tectonics, in Watters, T.R., and Schultz, R.A., eds., Planetary Tectonics: New York, Cambridge University Press, p. 121–182.

Watters, T.R., and Schultz, R.A., 2010, Planetary Tectonics: New York, Cambridge University Press, 518 p.

Watters, T.R., Solomon, S.C., Robinson, M.S., Head, J.W., André, S.L., Hauck, S.A., and Murchie, S.L., 2009, The tectonics of Mercury: The view after MESSENGER's first flyby: Earth and Planetary Science Letters, v. 285, p. 283–296, doi:10.1016/j.epsl.2009.01.025.

Watters, T.R., et al., 2010, Evidence of recent thrust faulting on the Moon revealed by the Lunar Reconnaissance Orbiter Camera: Science, v. 329, p. 936–940, doi:10.1126/science.1189590.

Watters, T.R., Robinson, M.S., Banks, M.E., Tran, T., and Denevi, B.W., 2012, Recent extensional tectonics on the Moon revealed by the Lunar Reconnaissance Orbiter Camera: Nature Geoscience, v. 5, p. 181–185, doi:10.1038/ngeo1387.

Weber, R.C., Bills, B.G., and Johnson, C.L., 2009, Constraints on deep moonquake focal mechanisms through analyses of tidal stress: Journal of Geophysical Research, v. 114, E05001, doi:10.1029/2008JE003286.

Williams, J.G., and Boggs, D.H., 2015, Tides on the Moon: Theory and determination of dissipation: Journal of Geophysical Research, v. 120, p. 689–724, doi:10.1002/2014JE004755.

Williams, N.R., Watters, T.R., Pritchard, M.E., Banks, M.E., Bell, J.F., III, and Tran, T., 2013, Fault dislocation modeled structure of lobate scarps from Lunar Reconnaissance Orbiter Camera digital terrain models: Journal of Geophysical Research, v. 118, p. 224–233, doi:10.1002/jgre.20051.

Geology

Global thrust faulting on the Moon and the influence of tidal stresses

Thomas R. Watters, Mark S. Robinson, Geoffrey C. Collins, Maria E. Banks, Katie Daud, Nathan R. Williams and Michelle M. Selvans

Email alerting services	click www.gsapubs.org/cgi/alerts to receive free e-mail alerts when new articles cite this article
Subscribe	click www.gsapubs.org/subscriptions/ to subscribe to Geology
Permission request	click http://www.geosociety.org/pubs/copyrt.htm#gsa to contact GSA

Notes

THE
GEOLOGICAL
SOCIETY
OF AMERICA

1

2 **GSA DATA REPOSITORY**

3 **Watters et al.**

4 **Digital Elevation Model**

5   A digital elevation model (DEM) for the Pasteur scarp (Fig. 1) was derived from

6 LROC NAC stereo pairs (Burns et al., 2012). These stereo pairs were initially processed

7 with the U.S. Geologic Survey's Integrated Software for Imagers and Spectrometers

8 (ISIS) and the terrain was derived using the BAE Systems SOCET SET® commercial

9 photogrammetry system (Miller and Walker, 1993, 1995) with custom libraries provided

10 by the USGS Astrogeology Science Center in Flagstaff, AZ. Profiles obtained from the

11 DEM show that the small, narrow graben in the back-scarp terrain are only a few meters

12 in depth at most. A topographic profile across one of the widest graben (~45 m) shows

13 that it is ~1.5 to 2 m deep with a relatively flat floor (Fig. DR1).

14 **Lobate Scarp Mapping**

15   The locations of lobate scarps are digitized as polylines (a connected series of

16 linear segments) at a scale of up to 1:20,000 in an equirectangular projection in equatorial

17 regions (between 60°N and 60°S). Digitization was completed on a 100m/pixel LROC

18 WAC monochrome (643 nm) mosaic and local area NAC mosaics sampled at 2 m/pixel.

19 NAC images with incidence angles between 50° and 80° were optimum for identifying

20 and digitizing the lobate scarps. Lobate scarps are often found in complexes or clusters

21 consisting of groups of individual scarps. Individual scarps were divided into segments

22 with uniform trends to best approximate the overall orientation and were digitized along

23 the base of the scarp face. The smallest digitized segments were ~200 m in length.

24   Image parameters important for the detection of tectonic landforms are incidence

25   angle, solar azimuth (illumination direction at the surface), and pixel scale. Incidence

26   angle is defined as the angle between the local solar vector and the surface normal.

27   Images obtained with low incidence angles (near local noon) are optimal for revealing

28   subtle reflectance variations (compositional or maturity differences) while images with

29   large incidence angle images (near terminator) are optimal for revealing subtle

30   topographic relief (e.g. tectonic landforms that have low relief and surface slopes of only

31   a few degrees). The illumination azimuth (compass direction towards sub-solar point) is

32   equally important to the detection of tectonic landforms because linear features with

33   orientations parallel to the solar azimuth may not be apparent (fewer shadows are being

34   cast). The orientations of the small-scale lobate scarps mapped in this study are

35   dominantly N–S at low to mid-latitudes and E–W at high latitudes. We considered that

36   this preferred orientation could be due to observational bias where features oriented

37   perpendicular to the local illumination direction are expected to be preferentially

38   enhanced, since at the equator the illumination direction is east or west and at the poles

39   the illumination direction is north or south. However, a plot of the mapped lobate scarp

40   segments with latitude shows that in addition to the ~20,000 fault scarp segments with

41   roughly N–S orientations ($\pm30°$) at low to mid-latitudes ($0°$ to $\pm60°$), there are also

42   ~7,900 segments with orientations of $\pm60°$ to $\pm90°$ (roughly E–W) at low to mid-latitudes

43   (Fig. DR2). At high latitudes (greater than $\pm60°$), there are ~4,300 scarp segments with

44   roughly E-W orientations along with ~1,800 segments with N–S orientations (Fig. DR2).

45   Further, a comparison of histograms of scarp segment lengths with E–W and N–S

46   orientations indicates no preference toward segments with greater lengths in the detection

47   of the scarps. Thus, while the effect of Sun azimuth bias cannot be discounted, the large

48   range of orientations at all latitudes suggests that it has not controlled our results.

49   **Orbital Recession and Diurnal Stress Models**

50   The stresses resulting from orbital recession were modeled using equations from

51   Melosh (1977, 1980). The maximum stresses at the sub- and anti-Earth points (at the tidal

52   axis) are given by

$$\sigma_{\theta\theta} = \frac{11}{3} E\left(\frac{1+\nu}{5+\nu}\right) h_2 \frac{M}{m} r^3 \left(\frac{1}{(a_o)^3} - \frac{1}{a^3}\right)$$

53   (1)

54

$$\sigma_{\varphi\varphi} = \frac{17}{3} E\left(\frac{1+\nu}{5+\nu}\right) h_2 \frac{M}{m} r^3 \left(\frac{1}{(a_o)^3} - \frac{1}{a^3}\right)$$

55   (2)

56

57   where $\sigma_{\theta\theta}$ and $\sigma_{\phi\phi}$ are the longitudinal (N-S) and latitudinal (E-W) stress components

58   respectively, E is Young's Modulus, ν is Poisson's ratio, M is the mass of the Earth, m is

59   the mass of the Moon, r is the radius of the Moon, and a_o is the starting orbital radius and

60   a is the current orbital radius. The magnitude of the orbital recession stresses are very

61   sensitive to h_2 and change in orbital radius a - a_o determined by the period of recession

62   (Fig. DR3).

63   The Earth-raised diurnal stresses on the Moon were modeled. At apogee, diurnal

64   stresses are compressional in the region around the sub-Earth and anti-Earth points (Fig.

65   DR4). However, diurnal stresses oscillate with the Moon's orbital position becoming

66   extensional at the same locations at perigee. Modeled orbital recession stresses plus

67   diurnal stress at apogee are superimposed on a background isotropic stress of 2 MPa

68 resulting from global contraction (Fig. DR5). The predicted fault trajectories correspond

69 to the orientation orthogonal to the most compressive stress directions of the recession

70 stresses. Deviations between the predicted and observed orientations may be due to a

71 variety of influences that include mechanical inhomogeneities associated with impact

72 basins. Significant deviations may also occur where the differential stress, the difference

73 in magnitude between the most and least compressive, are low. This is generally the case

74 at high latitudes (Fig. DR5).

75

76

77 Figure DR1. Topographic profile across the one of the widest graben in the back-scarp

78 terrain of the Pasteur scarp. Profile location is shown Fig. 1. Vertical exaggeration is

79 ~11:1. Elevations are referenced to a sphere of 1,737,400 m.

80

81 Figure DR2. Plot of orientations of all digitized lobate scarp segments as a function of

82 latitude. In the plot, 0° azimuth is N-S and ±90° azimuth is E-W. The plot shows there

83 are a large number of segments with orientations between ±30° (roughly N-S)

84 particularly at the low to mid-latitudes. However, the plot also shows a very large number

85 of segments with roughly N-S orientations (±30°) and E-W orientations (±60° to ±90°) at

86 all latitudes.

87

88 Figure DR3. Plot of the magnitude of the orbital recession stress verses h_2. Maximum

89 longitudinal component of the recession stress at the sub- and anti-Earth points are

90 determined for a range of recession periods using equation 2.

91

92 Figure DR4. Orientations of principal stresses due to Earth-raised diurnal tides at apogee.

93 Compressional stress components are show by red lines and reach a maximum of 5 kPa.

94 Extensional stress components are shown by blue lines. Diurnal stresses are modeled

95 with no latitude or longitude offset from the sub-Earth point. Sub-Earth and anti-Earth

96 regions shown with black circles.

97

98 Figure DR5. Orientation of the maximum principal stress due to orbital recession with

99 diurnal stresses at apogee and global contraction superimposed. Orbital recession stresses

100 were estimated using $h_2 = 0.08$, recession period $= 1.2 \times 10^9$ yrs, average orbit radius $=$

101 3.847×10^8 km, orbit radius at apogee $= 4.054 \times 10^8$ km. The red dashes are the directions

102 of the most compressive stress. Contours are in kPa with black being most compressive

103 and blue being least compressive stress.

104

105 **REFERENCES CITED**

106 Burns K.N., Speyerer, E.J., Robinson, M.S., Tran, T., Rosiek, M.R., Archinal, B.A.,

107   Howington-Kraus, E., and the LROC Science Team, 2012, Digital elevation models

108   and derived products from LROC NAC stereo observations: International Archives of

109   the Photogrammetry, Remote Sensing and Spatial Information Sciences, XXXIX-B4,

110   XXII ISPRS Congress.

111 Miller, S.B., and Walker, A.S., 1993, Further developments of Leica Digital Photo-

112   grammetric Systems by Helava: ACSM/ASPRS Ann. Convention Exposition, Tech.
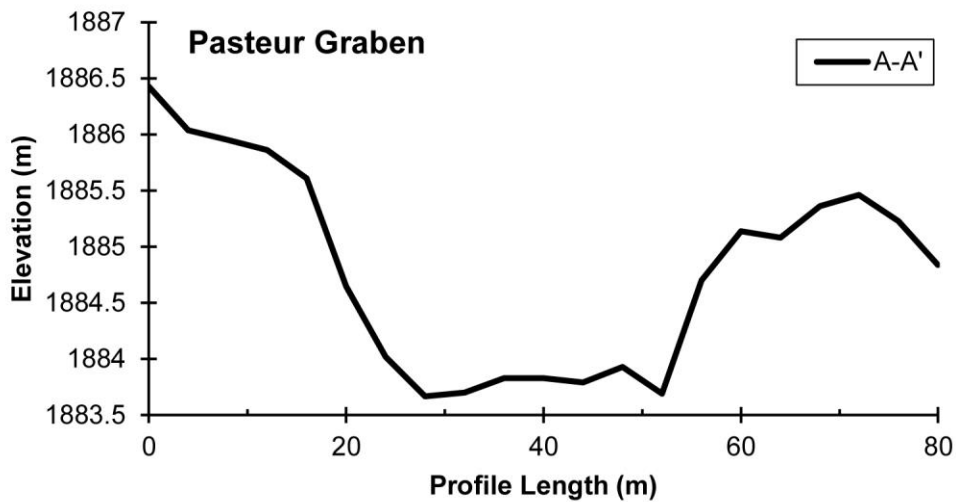
113   Papers, v. 3, p. 256–263.

114   Miller, S.B. and Walker, A.S., 1995, Die Entwicklung der digitalen photogrammetrischen

115   Systeme von Leica und Helava: Z. Photogramm. Fernerkundung, 1/95, p. 4-16.

116   Wahr, J., Selvans, Z.A., Mullen, M.E., Barr, A.C., Collins, G.C., Selvans, M.M., and

117   Pappalardo R.T., 2009, Modeling Stresses on Satellites due to Non-Synchronous

118   Rotation and Orbital Eccentricity Using Gravitational Potential Theory: Icarus, v.

119   200, p.188-206.

120   Weber, R., Lin, P-Y, Garnero, E.J., Williams, Q., and Lognonné, P., 2011, Seismic

121   Detection of the Lunar Core: Science, v. 331, p. 309-312.

122

Table DR1. Orientation Vectors of Lobate Scarps

Longitude (deg.)	Latitude (deg.)	Mean	Median	Weighted Mean	Standard Deviation	Sum of Lengths (km)
-160	-60	-8.44	21.04	-38.22	115.35	22.76
-160	-40	-10.83	23.98	-22.26	98.35	24.02
-160	-20	13.28	29.55	42.28	127.32	46.36
-160	0	13.82	13.24	14.87	103.37	167.55
-160	20	38.23	45.74	43.09	91.72	102.92
-160	40	38.93	62.75	43.61	96.61	226.2
-160	60	26.88	38	28.11	92.94	187.22
-160	80	19.42	41.5	28.67	90.28	31.72
-120	-80	51.87	69.92	49.23	77.39	29.3
-120	-40	-17.02	10.51	-14.43	81.5	53.3
-120	-20	8.39	18.22	13.35	103.21	67.08
-120	20	-27.64	-6.56	-23.18	115.9	33.43
-120	40	-20.52	-28.07	-19.46	97.09	139.64
-120	60	38.98	73.87	14.77	83.83	189.76
-120	80	-11.96	-23.76	-6.77	100.43	74.52
-80	-80	-37.58	-82.81	-13.16	86	36.78
-80	-60	48.01	90	47.47	103.23	130.5
-80	-20	-4.02	29.57	-13.68	86.69	7.88
-80	20	52.64	63.49	35.49	122.96	29.75
-80	40	92.94	127.48	89.62	98.95	57.2
-80	60	45.14	100.23	33.01	121.1	52.17
-80	80	7.04	31.28	8	70.89	20.39
-40	-80	1.02	0	1.87	149.56	4.25
-40	-60	44.86	30.46	34.61	115.91	30.07
-40	-40	0.71	17.48	-0.39	99.18	428.56
-40	-20	47.79	21.56	63.7	83.88	21.46
-40	0	49.71	36.53	46.08	100.95	71.29
-40	20	15.56	-18.01	31.81	92.27	56.69
-40	40	-14.78	-155.94	-25.67	166.81	5.08
-40	60	50.86	77.27	44.11	86.94	62.53
-40	80	67.16	100.3	63.94	89.63	218.11
0	-80	17.14	65.24	30.89	96.5	78.66
0	-60	11.03	49.31	1.09	97.05	135.53
0	-40	37.49	41.44	37.6	107.11	130.94
0	-20	57.03	119.92	52.9	113.99	34.66
0	0	1.61	3.8	1.76	115.29	257.69
0	20	14.6	29.72	27.14	110.75	123.15

0	40	1.14	13.05	6.53	112.44	202.2
0	60	36.1	68.23	35.98	106.5	88.85
0	80	23.39	47.7	21.56	83.53	98.83
40	-80	15.04	43.58	14.27	90.91	37.31
40	-60	-16.77	24.57	1.09	109.13	63.49
40	-40	-19.03	14.49	-20.11	102.33	103.56
40	-20	27.37	17.56	29.46	90.97	140.17
40	0	39.54	48.02	47.23	127.99	100.14
40	20	26.39	17.75	22.11	96.1	180.83
40	40	23.41	23.58	22.99	110.09	130.49
40	60	-34.71	-60.88	-35.09	90.27	71.24
40	80	-42.74	-77.99	-33.63	88.01	92.2
80	-60	4.18	-15.56	10.23	139.2	52.15
80	-40	47.27	42.66	50.18	93.72	82.83
80	-20	-7.17	8.78	-1.59	124.97	97.72
80	0	13.73	13.87	2.83	116.9	124.47
80	20	-4.66	4.64	-2.3	127.92	27.21
80	40	-7.27	1.37	-1.49	128.67	154.92
80	60	110.17	131.32	109.81	75.94	31.74
80	80	95.38	105.05	98.42	58.51	21.28
120	-80	-96.01	-128.27	-88.66	86.94	17.95
120	-60	0.16	2.3	-2.81	98.72	152.24
120	-40	60.43	79.45	68.27	92.86	160.53
120	-20	25.25	33.65	23.39	108.42	267.77
120	0	-12.34	4.65	-29.7	114.52	90.3
120	20	26.77	32.72	26.2	125.07	148.84
120	40	65.67	87.43	54.95	76.62	100.22
120	60	6.6	30.42	-19.76	119.76	11.4
120	80	-72.85	-109.89	-81.79	97.53	194.98
160	-60	-0.92	24.11	-0.45	69.27	20.73
160	-40	42.37	48.33	50.27	97.14	187.2
160	-20	-7.28	15.41	-12.86	124.61	98.21
160	0	20.39	17.21	16.54	117.99	317.86
160	20	62.89	123.86	76	109.57	122.32
160	40	31.87	65.9	28.84	99	243.47
160	60	21.76	32.51	-1.76	85.03	118.83
160	80	-34.92	-62.97	-34.2	95.38	164.71

123 Longitudes and latitudes give the location centers of sampling areas. North is equal to 0 degrees. The
124 accuracy of mean, median, and weighted mean values for the orientation vectors were check by direct
125 comparison with digitized polylines.
126

127

128   Figure DR1.

Orientations of Digitized Segments

129

130   Figure DR2.

Recession Stress ($\sigma_{\varphi\varphi}$)
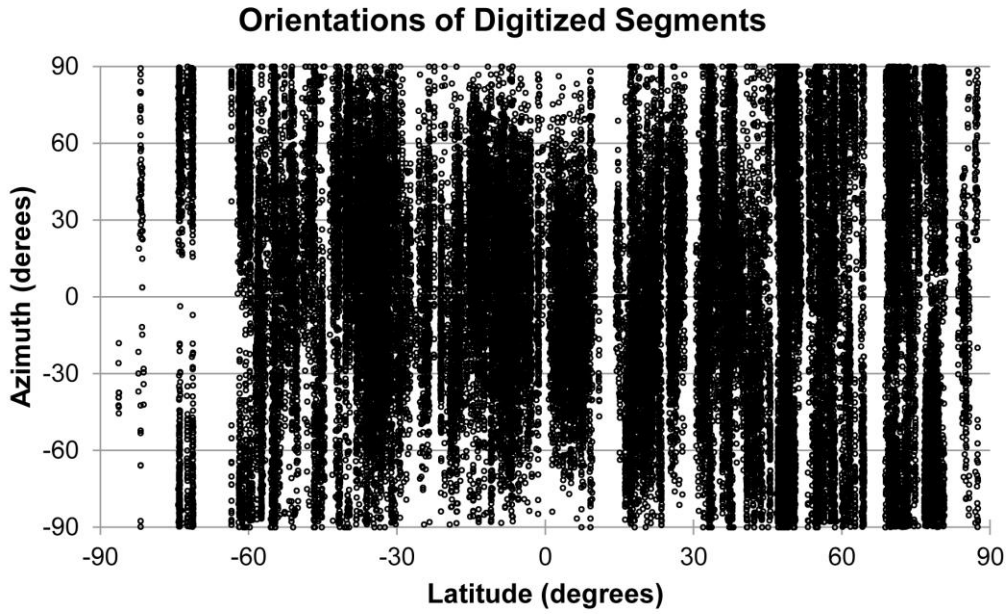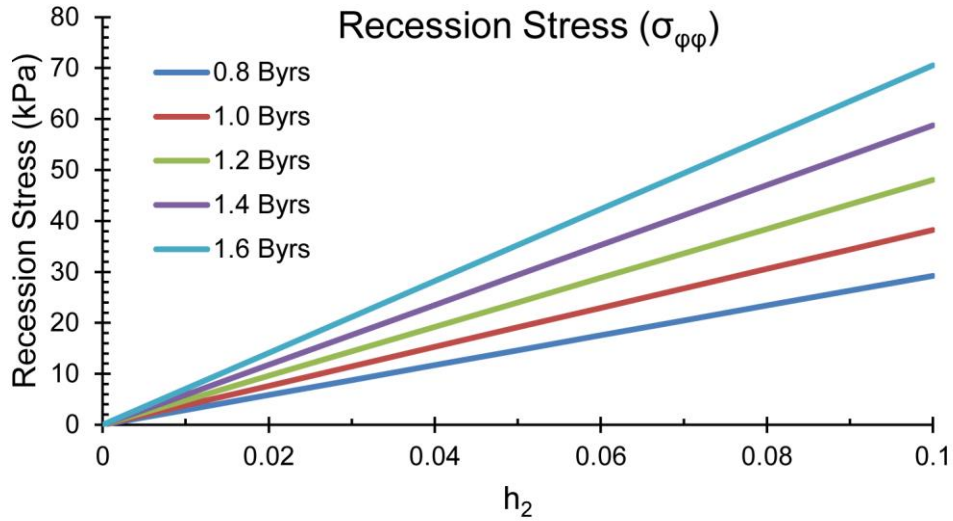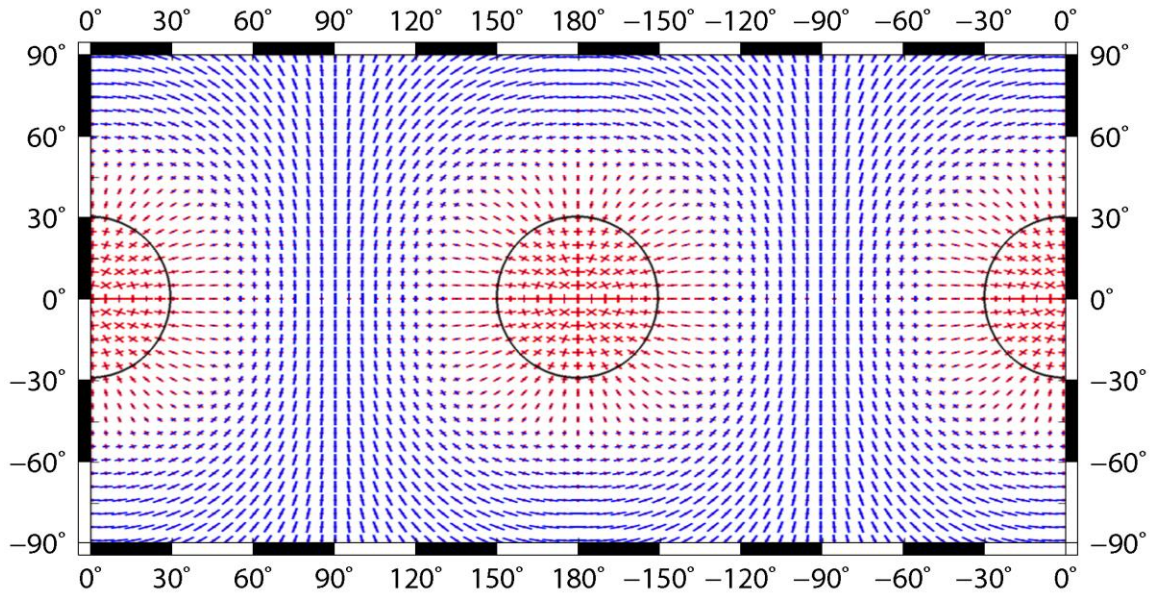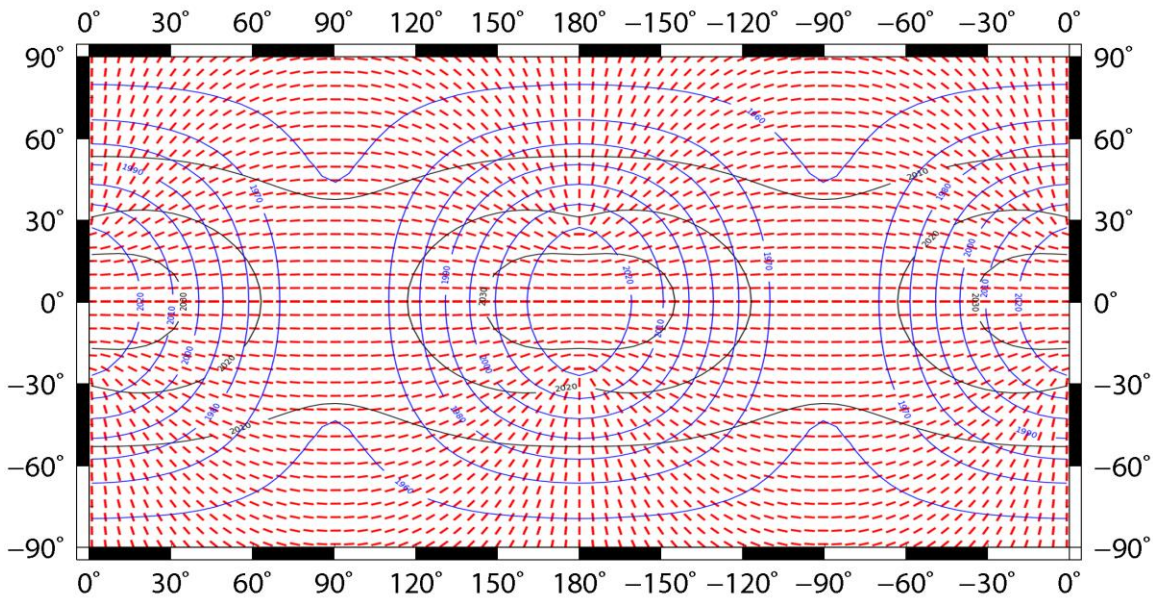
131

132   Figure DR3.

133

134   Figure DR4.

135

136

137   Figure DR5.